Monthly Notices of the ROYAL ASTRONOMICAL SOCIETY

MNRAS **536,** 2558–2571 (2025) https://doi.org/10.1093/mnras/stae2704
Advance Access publication 2024 December 12

Uniform characterization of an ensemble of main-sequence benchmark stars: effect of *Gaia*-based data on grid search models

Benard Nsamba [1,2,3]★ Achim Weiss [1] and Juma Kamulali[2]

[1]*Max-Planck-Institut für Astrophysik, Karl-Schwarzschild-Str 1, D-85748 Garching, Germany*
[2]*Department of Physics, Faculty of Science, Kyambogo University, P.O. Box 1, Kyambogo, Kampala, Uganda*
[3]*Instituto de Astrofísica e Ciências do Espaço, Universidade do Porto, Rua das Estrelas, PT4150-762 Porto, Portugal*

Accepted 2024 December 5. Received 2024 November 23; in original form 2023 December 19

ABSTRACT

The inference of stellar parameters (such as radius and mass) through asteroseismic forward modelling depends on the number, accuracy, and precision of seismic and atmospheric constraints. ESA's *Gaia* space mission is providing precise parallaxes which yield an additional constraint to be included in the model grid search. Using a handful of main-sequence benchmark stars, we perform a uniform characterization of these stars. We assess the accuracy and precision of stellar parameters inferred from grid-based searches when a *Gaia*-based luminosity is combined with different stellar constraints. We also examine the precision needed for an interferometric radius (model-independent radius) to have a significant contribution towards the determination of stellar mass in the optimization process. Our findings show that more precise stellar masses are inferred for some stars when seismic and spectroscopic constraints are complemented with a *Gaia*-based luminosity, with a scatter varying from 1.9 per cent to 0.8 per cent. However, the inferred stellar radii are underestimated when compared to the interferometric radii and yield a scatter of $\sim$1.9 per cent. In addition, we demonstrate that a precisely measured interferometric radius ($\lesssim$1 per cent) when applied in the optimization process yields a mass with a precision $\lesssim$1.5 per cent. Finally, we find that when only $l = 0$ mode oscillation frequencies are available, robust masses and radii are still attainable. However, this requires precise and numerous $l = 0$ mode oscillations frequencies (>8) to be coupled with atmospheric constraints.

Key words: asteroseismology – stars: fundamental parameters – stars: oscillations.

1 INTRODUCTION

Asteroseismology is a powerful tool used to characterize stellar interior structures, test the understanding and description of stellar physics, and infer fundamental stellar properties such as the mean density, radius, mass, and age, (e.g. Miglio & Montalbán 2005; Metcalfe et al. 2010, 2014; Silva Aguirre et al. 2011; Creevey et al. 2012; Doğan et al. 2013; Valle et al. 2014, 2015, 2019; Davies et al. 2015; Silva Aguirre et al. 2015; Deal et al. 2018, 2020; Nsamba et al. 2018a, b, 2019; Moedas, Nsamba & Clara 2020). The knowledge of the fundamental stellar properties has been employed in making essential contributions towards the understanding of other astrophysics research fields such as Galactic archaeology (e.g. Miglio et al. 2017; Döner et al. 2023) and Exoplanet studies (e.g. Huber et al. 2009, 2019; Benomar et al. 2014; Lebreton, Goupil & Montalbán 2014; Metcalfe et al. 2014; Campante et al. 2016, 2019; Lundkvist et al. 2016; Jiang et al. 2020; Nielsen et al. 2020, just to mention a few).

The continuous advancement of asteroseismiology research is greatly attributed to a handful of space missions such as the French led CoRoT (Convection, Rotation, and Planetary Transits; Auvergne et al. 2009) mission, NASA's *Kepler* space mission (Borucki et al. 2010), NASA's *TESS* (*Transiting Exoplanet Survey Satellite*; Ricker et al. 2014) mission, and with the future ESA PLATO (PLAnetary Transits and Oscillations of stars; Rauer et al. 2014) mission. This is partly because space missions provide uninterrupted photometric data with significantly minimized noise levels, yielding a frequency spectrum with a range of excited modes which can be easily identified (see Kjeldsen & Bedding 2004, 2005). The exceptional photometric observations have given rise to continuous development of asteroseismic tools which have been employed successfully to infer precise star parameters like radius, mass, and age (e.g. Bellinger et al. 2017; Salmon et al. 2021; Guo & Jiang 2023). The systematic uncertainties (scatter) on stellar parameters derived using different seismic optimization tools have also been explored (see Monteiro 2009; Silva Aguirre et al. 2015, 2017). Furthermore, extensive exploration of the impact of model physics such as atomic diffusion including gravitational settling (Valle et al. 2014, 2015; Nsamba et al. 2018a), radiative acceleration (Deal et al. 2018, 2020; Moedas et al. 2020), solar metallicity mixtures (Nsamba et al. 2018b; 2019; Valle et al. 2019), opacities (Huebner & Barfield 2014), equation of states (Rogers & Iglesias 1998), rotational mixing, semi-convection, core, and envelope convective overshooting (Miglio & Montalbán 2005; Silva Aguirre et al. 2011; Creevey et al. 2012; Valle et al. 2015; Ahlborn et al. 2022), on the derived stellar parameters have also been a centre of attention for about a decade or so. All these efforts have generated a leap forward in our understanding of additional uncertainties to be considered on stellar parameters derived using asteroseismology.

★ E-mail: nsamba@mpa-garching.mpg.de

Fundamental stellar parameters inferred using asteroseismology are commonly based on 'forward modelling techniques'. This involves building dedicated internal structure models which represent the targeted/observed star. This is also known as 'a'la carte modelling' (Lebreton et al. 2014). Based on a set of available observational stellar data, an optimization process is carried out to determine the stellar model which best matches the available data. There are two sets of observational data usually considered in the optimization process, i.e. seismic data that include global oscillation parameters (i.e. frequency of maximum power, $\nu_{\rm max}$, and large frequency separation, $\Delta\nu$), individual oscillation frequencies, $\nu_{\rm i}$, or their combinations (Roxburgh & Vorontsov 2003), and classical constraints composed of effective temperature, $T_{\rm eff}$, metallicity, [Fe/H] or individual abundances, luminosity, L, and when available a model-independent radius, R. Although this approach is known to yield precise stellar parameters, one has to keep in mind that the inferred stellar parameters are model-dependent and therefore sensitive to the input physics used in the models (e.g. Silva Aguirre et al. 2015; Nsamba et al. 2018a; Moedas et al. 2022).

With the tremendous success of asteroseismic techniques towards the determination of stellar parameters, it is relevant to establish the accuracy and precision of asteroseismic inferences. Silva Aguirre et al. (2017) explored the robustness of asteroseismically determined stellar parameters for a sample of 66 *Kepler* Legacy stars whose individual oscillation frequencies are available. They demonstrated that the uncertainties on derived mass, radius, and age are reduced when individual oscillation frequencies are taken into account compared to when only seismic global parameters (i.e. frequency of maximum power, $\nu_{\rm max}$ and large frequency separation, $\Delta\nu$) are considered (Gilliland et al. 2010), i.e. from 2.2 to 2.0 per cent in radius, 5.4 to 4.0 per cent in mass, and 25 to 10 per cent in age, respectively. However, this improvement in the precision of asteroseismically determined stellar parameters also necessitates corresponding tests on accuracy of these parameters. These tests can only be achieved when compared to corresponding model-independent parameters with uncertainties (both statistical and systematic) smaller than the asteroseismically determined stellar parameters (Cunha et al. 2021).

Long-baseline interferometry is reported to be successful in estimating angular diameters of bright stars, from which their corresponding radii are derived (e.g. Kervella et al. 2003; Mazumdar et al. 2009; Creevey et al. 2012, 2015; Huber et al. 2012a; Ligi et al. 2016; Pourbaix & Boffin 2016; Kervella et al. 2017; Karovicova et al. 2020). This has been used to test the precision and accuracy of stellar radii inferred using asteroseismology (e.g. Huber et al. 2012a, b; White et al. 2013, 2015). For instance, through the combination of *Hipparcos* parallaxes with angular diameters of five main-sequence stars, Huber et al. (2012a) calculated model-independent linear radii of these stars and compared them with asteroseismic radii (i.e. based on asteroseismic scaling relations for the frequency of maximum power, $\nu_{\rm max}$, and the large frequency separation, $\Delta\nu$). They report the asteroseismic radii to be accurate to better than 4 per cent. In addition, they anticipate improvement in the accuracy of asteroseismic radii when determined through detailed modelling involving individual oscillation frequencies.

To quantify the accuracy of seismic masses, model-independent masses are needed. Stars in binary systems offer a great opportunity of availing model-independent masses if their orbital parameters are known. The limitation to performing this exercise is that only a handful of main-sequence benchmark stars are available with both seismic and model-independent parameters, like radius and mass. To this end, previous efforts concentrated on studies of double-lined spectroscopic binaries and eclipsing binaries (e.g. Torres, Andersen & Giménez 2010; Halbwachs et al. 2020; Serenelli et al. 2021; Beck et al. 2023). In the context of exploring the robustness of stellar parameters expected from the future ESA's PLATO mission, Cunha et al. (2021) performed a 'hare-and-hounds exercise' that involved inferring stellar parameters of six simulated (artificial) main-sequence stars. They reported a difference in the accuracy between simulated and 'true values' in radius, mass, and age to be 1.33, 4.32, and 11.25 per cent, respectively. We highlight that the simulated models may already have suffered from incorrect physics that would reduce the accuracy of models of real stars even further. In addition, Cunha et al. (2021) also examined how the precision and accuracy of inferred parameters would vary when different surface corrections routines and classical combinations are adopted. Creevey et al. (2007) used simulated data and explored the relevance of a model-independent radius and its combination with other stellar constraints (seismic and classical) towards the determination of a precise and accurate stellar mass. Their findings illustrate that a model-independent radius when included in the optimization process plays a significant role towards the determination of a precise and accurate stellar mass.

ESA's *Gaia* provides unprecedented quantity and quality of a uniform, homogeneous, and precise data set for more than a billion stars, yielding their accurate astrometric data (Gaia Collaboration et al. 2018, 2023). Huber et al. (2017) highlight an insightful glimpse of the powerful synergy between *Gaia* and asteroseismology. Using 2200 *Kepler* stars at different evolution phases (i.e. from the main sequence to red-giant branch), they presented a comparison of radii based on *Gaia* DR1 parallaxes and asteroseismic scaling relations – thus demonstrating that asteroseismic radii determined using scaling relations are accurate to ∼5 per cent for stars between 0.8 and 8 $R_{\odot}$. Furthermore, using an extended sample of ∼3900 *Kepler* mission stars, of which ∼300 stars are dwarfs and subgiants and ∼3600 are first-ascent giants ranging between 0.8 and 30 $R_{\odot}$, Zinn et al. (2019) report a 2 per cent agreement between radii based on *Gaia* parallax to radii based on asteroseismic scaling relations, further illustrating the accuracy and precision of scaling relations.

Gaia data allow stellar luminosities to be obtained based on their precise parallax measurements – providing an additional constraint whose impact in the model grid search needs to be examined. The main aim of this article is two folds: we carry out a uniform characterization of an ensemble of main-sequence benchmark stars and (i) assess the relevance of a stellar luminosity (i.e. derived based on parallax measurement) towards the determination of stellar parameters, mainly radius and mass and (ii) we determine the contribution of a model-independent radius measurement towards the estimation of a precise and accurate stellar mass. Finally, we examine the precision needed for an interferometric radius (model-independent radius) to have an influential impact towards the determination of stellar mass in the optimization process.

2 STELLAR MODEL GRID AND BENCHMARK STARS

2.1 Stellar model grid

We employed the one dimensional (1D) stellar code MESA (Modules for Experiments in Stellar Astrophysics Paxton et al. 2011, 2013, 2015, 2018, 2019) version r12778 for the computation of stellar models. The computed stellar model grid is made up of main-sequence stellar evolution tracks running from the zero-age main-sequence (ZAMS) phase to the end of the main-sequence phase, spanning the parameter space in mass, M, [0.7–1.6] $M_{\odot}$ in steps

Table 1. Selected benchmark stars, their commonly used nomenclature, corresponding spectroscopic constraints (metallicities, [Fe/H], and effective temperatures, $T_{\rm eff}$) and interferometric radii, R. The second column represents the *Kepler* Input Catalogue (KIC) name while the third column indicates that adopted in the plots in this article.

Target star	KIC	Used ID	[Fe/H] (dex)	$T_{\rm eff}$ (K)	R ($R_\odot$)
16 Cyg A	12 069 424	Cyg A	0.10 ± 0.03^{b}	5825 ± 50^{b}	1.220 ± 0.020^{a}
16 Cyg B	12 069 449	Cyg B	0.05 ± 0.02^{b}	5750 ± 50^{b}	1.120 ± 0.020^{a}
Doris	8 006 161	Doris	0.34 ± 0.10^{c}	5466 ± 77^{c}	0.952 ± 0.021^{d}
Perky	6 106 415	Perky	-0.04 ± 0.10^{c}	6037 ± 77^{c}	1.289 ± 0.037^{d}
Saxo2	6 225 718	Saxo2	-0.07 ± 0.10^{c}	6313 ± 76^{c}	1.306 ± 0.047^{d}
α Centauri A	–	Cen A	0.23 ± 0.05^{e}	5832 ± 62^{e}	1.2234 ± 0.0053^{e}
α Centauri B	–	Cen B	0.23 ± 0.05^{e}	5795 ± 19^{e}	0.8632 ± 0.004^{e}
Sun	–	Sun	0.00 ± 0.05	5777 ± 50^{g}	1.000 ± 0.0004^{f}

[a]White et al. (2013),
[b]Ramírez et al. (2009),
[c]Buchhave & Latham (2015),
[d]Huber et al. (2012b),
[e] Nsamba et al. (2018b),
[f] Meftah, M. et al. (2018),
[g] Prša et al. (2016).

of 0.05 $M_\odot$, initial metallicity, [Fe/H], [−0.50–0.50] dex in steps of 0.1, and the helium enrichment ratios[1], $\Delta Y/\Delta Z$, from [0.4–2.4]. The initial helium mass fractions, $Y_{\rm i}$ is determined following the expression

$$Y_{\rm i} = \left(\frac{\Delta Y}{\Delta Z}\right) Z_{\rm i} + Y_0 \ , \tag{1}$$

where $Z_{\rm i}$ is the initial metal mass fraction and Y_0 is the primordial big bang nucleosynthesis helium mass fraction value taken as 0.2484 (Cyburt, Fields & Olive 2003). For each stellar model, we calculated the corresponding adiabatic theoretical oscillation frequencies for spherical degrees $l = 0$, 1, 2, and 3, using the GYRE oscillation code (Townsend & Teitler 2013).

The global input physics of our stellar grid includes NACRE (Nuclear Astrophysics Compilation of REaction rates; Angulo et al. 1999) reaction rates with specific rates for ^{14}N(p, γ)^{15}O described by Imbriani et al. (2005). In addition, the grid used the 2005 updated version of the OPAL equation of state (Rogers & Nayfonov 2002). At high temperatures, OPAL tables (Iglesias & Rogers 1996) were used to cater for opacities, while tables from Ferguson et al. (2005) were used for lower temperatures. Furthermore, our grid takes into account solar chemical mixtures from Asplund et al. (2009). The surface boundary of generated stellar models was described using the Krishna-Swamy atmosphere (Krishna Swamy 1966). We also follow the prescription of Cox & Giuli (1968) in the treatment of convection, and employ a solar calibrated mixing length parameter, $\alpha_{\rm MLT}$ of 1.71. We note that atomic diffusion (gravitation settling component only; Thoul, Bahcall & Loeb 1994) was considered in stellar models which do not demonstrate overdepletion at the stellar surface (i.e. models $\lesssim$1.2 $M_\odot$). Lastly, for the stellar models with convective cores, we included convective core overshoot using the exponential decay with a diffusion coefficient described by Herwig (2000)

$$D_{\rm ov} = D_0 \exp\left(-\frac{z}{f H_{\rm p}}\right) \ , \tag{2}$$

where f is the overshoot parameter and restricted to 0.01, $H_{\rm p}$ is the pressure scale height, D_0 is the diffusion coefficient of the unstable convective region, and z is the distance from the boundary of the convective region.

[1]We note that the range of helium enrichment ratio used also includes the solar value of 1.23 deduced from our solar calibration procedures.

2.2 Benchmark stars

Our selected stellar sample is restricted to only main-sequence stars within the mass range [0.7–1.6] $M_\odot$ and either having a model-independent radii and/or mass available. Table 1 shows the list of our benchmark stars, their corresponding adopted nomenclature, spectroscopic constraints (metallicities, [Fe/H], and effective temperatures, $T_{\rm eff}$), and interferometric radii. We also include the Sun-as-a-star among the benchmark stars. This is because the Sun is one of the best characterized stars which displays a rich spectrum of excited oscillation modes with extremely high signal-to-noise ratios. The adopted solar frequencies are from Lund et al. (2017), whose quality is similar to that of *Kepler* space mission. For the purpose of this work, this is relevant because it allows us to treat the Sun as a '*Kepler* observed star', hence assessing the precision and accuracy of the inferred parameters in a similar manner as for the other selected benchmark stars in Table 1. We now highlight the available essential stellar properties of each of our stars:

(i) 16 Cyg A (HD 186408, HR 7503, KIC 12069424) and B (HD 186427, HR 7504, KIC 12069449) are binary star systems whose angular diameters have been measured by White et al. (2013), based on observations using long-baseline optical interferometry with the Precision Astronomical Visible Observations (PAVO; Ireland et al. 2008) beam combiner at the High Angular Resolution Astronomy (CHARA; ten Brummelaar et al. 2005) Array. White et al. (2013) found the angular diameters of 16 Cyg A and B to be 0.539 ± 0.007 mas and 0.490 ± 0.006 mas, respectively. In addition, through the combination of interferometric diameters with *Hipparcos* parallax measurements, they measured a linear radius of 1.22 ± 0.02 $R_\odot$ and 1.12 ± 0.02 $R_\odot$ for 16 Cyg A and B, respectively. Unfortunately, 16 Cyg A and B have long orbital periods estimated to be over 18 000 yr (Hauser & Marcy 1999), and therefore no dynamical masses are available. It is also worth noting that 16 Cyg B hosts a Jovian-mass companion planet whose mass is estimated to be 1.5 MJ (Cochran et al. 1997).
16 Cyg A and B are well-studied solar analogues following the continuous *Kepler* space observation for about 2.5 yr, providing high-quality seismic data, allowing for the extraction of over 48

oscillation frequency modes (Lund et al. 2017). This leads to a series of detailed seismic studies ranging from those involving testing asteroseismic tools which employ different optimization techniques (such as machine leaning, Bayesian techniques; Metcalfe et al. 2012; Bellinger et al. 2017; Silva Aguirre et al. 2017; Farnir et al. 2020), analysis of acoustic glitch signatures aimed at constraining the surface helium abundances (e.g. Verma et al. 2014), to constraining core properties such as core hydrogen abundances (Nsamba et al. 2022).

(ii) α Centauri system is the brightest, closest triple star system to our Sun. It consists of Proxima Centauri (HIP 70890) and a binary component made of solar-type stars, i.e. α Centauri A (HD 128620, HR 5459) and B (HD 128621, HR 5460). This binary component provides a unique opportunity for testing and improving our understanding of stellar interior physics. This is attributed to the wealth of available highly precise observations, namely, interferometric radii ($R_{\rm A} = 1.2234 \pm 0.0053\,{\rm R}_{\odot}$ and $R_{\rm B} = 0.8632 \pm 0.004\,{\rm R}_{\odot}$; Kervella et al. 2017), dynamical masses ($M_{\rm A} = 1.1055 \pm 0.004\,{\rm M}_{\odot}$ and $M_{\rm B} = 0.9373 \pm 0.003\,{\rm M}_{\odot}$; Kervella et al. 2017), precise parallax measurements (747.1± 1.2; Söderhjelm 1999, 743 ± 1.3; Pourbaix & Boffin 2016, 747.12 ± 0.61; Kervella et al. 2016), and asteroseismic data from a handful of ground-based surveys (Bouchy & Carrier 2002; Bedding et al. 2004, 2005; Kjeldsen et al. 2005; de Meulenaer et al. 2010; Bazot, Bourguignon & Christensen-Dalsgaard 2012). Table 1 also shows the metallicity and effective temperatures adopted for α Centauri A and B.

α Centauri binary system has been used as a test-bed for stellar model physics because of the precisely available observational constraints (Eggenberger et al. 2004; Miglio & Montalbán 2005; Yıldız 2007; Joyce & Chaboyer 2018). In fact, enormous efforts have been dedicated towards ascertaining the nature of the core of one of the binary components, α Centauri A. This is because its dynamical mass (1.1 $\rm M_{\odot}$) lies in the mass region where stars are expected to develop a convective core while on the main sequence, i.e. 1.1–1.2 $\rm M_{\odot}$ (see details in Bazot et al. 2012, 2016; Nsamba et al. 2018b, 2019; Salmon et al. 2021). The disagreements in the predictions of the convective/radiative nature of the core of α Centauri A is expected to be resolved when more precise oscillation frequencies are made available.

(iii) KIC 8 006 161 (HD 173701), also famously known as Doris, is a metal-rich seismic solar analogue with both spectroscopic ground-based observations (Karoff et al. 2018) and up-to 2.5 yr of continuous *Kepler* observations (Lund et al. 2017). The angular diameter measurements of Doris have been measured by Huber et al. (2012b), yielding an interferometric radius of 0.952 ± 0.021 $\rm R_{\odot}$. Doris is also reported to have a high metallicity of [Fe/H] = 0.34 ± 0.1 dex and an effective temperature of 5488 ± 77 K (Buchhave & Latham 2015). These sets of constraints and characteristics of Doris make it an interesting benchmark solar-like main-sequence star. Due to its high metallicity, various studies have not only focused on deriving the fundamental stellar properties of Doris (e.g. Basu & Kinnane 2018), but have also been directed towards examining its magnetic activity cycle (Kiefer et al. 2017; Santos et al. 2018, 2023; Kiefer & Broomhall 2020). The latter is because of the variations in opacity and convection zone depth attributed to its high metallicity.

(iv) KIC 6 106 415 (HD 177153) and KIC 6 225 718 (HD 187637) are commonly known as Perky and Saxo2, respectively. These two stars are part of the *Kepler* Legacy sample stars with high-quality sesimic data (Lund et al. 2017; Silva Aguirre et al. 2017). Mathur et al. (2012) analysed a group of 22 stars (including KIC 6106415) using the Asteroseismic Modelling Portal (AMP; Metcalfe & Charbonneau 2003; Metcalfe, Townsend & Ball 2023). Interestingly, they reported the initial helium abundance of KIC 6 106 415 to be consistent with the primordial helium abundance of 0.246, while Verma et al. (2019) determined the envelope helium abundance of KIC 6 106 415 through the analysis of a glitch signature arising from the ionization of helium and found it to span the range [0.201–0.222]. This disagreement in the initial helium abundance has a direct impact on the inferred stellar mass as illustrated in Nsamba et al. (2021). The interferometric radii measurements of KIC 6 106 415 and KIC 6 225 718 are available from Huber et al. (2012a), i.e. 1.289 ± 0.037 $\rm R_{\odot}$ and 1.306 ± 0.047 $\rm R_{\odot}$, respectively. KIC 6 106 415 has a metallicity of −0.04 ± 0.1 dex and effective temperature of 6037 ± 77 K (Buchhave & Latham 2015). KIC 6 225 718 is also reported to have a metallicity of −0.07 ± 0.1 dex and effective temperature of 6313 ± 76 K (Buchhave & Latham 2015).

2.3 *Gaia* parallax-based luminosities and radii

Table 2 shows the *Gaia* parallax measurements for our stellar sample. Among the benchmark stars, α Centauri A and B do not have any *Gaia* parallax values available. This is attributed to the high brightness and binary nature of the α Centauri A and B system which limits the absolute accuracy of *Gaia* custom data reduction processes (Akeson et al. 2021). Therefore, we adopt the available parallax measurements of α Centauri A and B from *Hipparcos* data (van Leeuwen 2007).

The parallax-based luminosities (L) for our benchmark stars were calculated using the expression (Pijpers, F. P. 2003)

$$\log\left(\frac{L}{L_{\odot}}\right) = 4 + 0.4M_{\rm bol,\odot} - 2\log\pi\,[\rm mas] - 0.4(V - A_{\rm v} + {\rm BC_v})\,, \quad (3)$$

where $M_{\rm bol,\odot}$ is the solar bolometric magnitude approximated to 4.73 based on Torres et al. (2010), π_{Gaia} and $\pi_{Hipparcos}$ are parallaxes obtained from *Gaia* DR3 data release[2] and *Hipparcos* data[3], respectively. For comparison purposes, we also determine the luminosity values for our target stars based on their corresponding *Hipparcos* parallax measurements (see Table 2 and Fig. 1). V is the visual magnitude obtained from the same *Hipparcos* data base. The bolometric corrections, $\rm BC_v$, were calculated from polynomials expressed as functions of stellar effective temperatures as suggested by Flower (1996) and corrected by Torres et al. (2010). The stellar extinction in the V band, $A_{\rm v}$, was determined using the expression

$$A_{\rm v} = R \times E(B - V)\,, \quad (4)$$

where R is the reddening constant of 3.1 adopted based on Fitzpatrick (1999) and $E(B - V)$ is the colour excess, obtained using STILISM[4] (STructuring by Inversion the Local Intersteller Medium: Lallement et al. 2014; Capitanio et al. 2017).

Fig.1 shows a comparison of the derived luminosities based on *Gaia* and *Hipparcos* parallaxes, with the bottom panel showing their fractional differences with a scatter of ∼1.4 per cent and an offset of −0.5 ± 0.6 per cent. From Table 2, it is evident that the *Gaia* parallax measurements are more precise compared to the *Hipparcos* parallaxes; however, this barely translates into somewhat more precise *Gaia*-based luminosities compared to *Hipparcos*-based

[2]https://gea.esac.esa.int/archive/
[3]http://vizier.cds.unistra.fr/viz-bin/VizieR?-source = V/137D/XHIP
[4]https://stilism.obspm.fr/

Table 2. Parallax-based luminosities for our sample stars. The eighth column shows the radii values deduced in this work using equation 5.

Target Star	π_{Gaia} (mas)	$\pi_{Hipparcos}$ (mas)	$V_{\rm mag}$	$E(B-V)$	L_{Gaia} ($L_\odot$)	$L_{Hipparcos}$ ($L_\odot$)	R ($R_\odot$)
16 Cyg A	47.32 ± 0.02	47.44 ± 0.27	5.99	0.001 ± 0.015	1.50 ± 0.06	1.49 ± 0.07	1.225 ± 0.014
16 Cyg B	47.33 ± 0.02	47.14 ± 0.27	6.25	0.001 ± 0.015	1.19 ± 0.05	1.20 ± 0.05	1.113 ± 0.014
Doris	36.99 ± 0.02	37.47 ± 0.49	7.54	0.002 ± 0.015	0.63 ± 0.03	0.61 ± 0.03	0.965 ± 0.017
Perky	24.16 ± 0.01	24.11 ± 0.44	7.20	0.004 ± 0.015	1.85 ± 0.08	1.86 ± 0.10	1.286 ± 0.0267
Saxo2	19.01 ± 0.02	19.03 ± 0.46	7.53	0.004 ± 0.015	2.14 ± 0.09	2.14 ± 0.14	1.307 ± 0.034
α Centauri A	–	742.12 ± 1.40	−0.01	0.000 ± 0.014	–	1.53 ± 0.06	–
α Centauri B	–	742.12 ± 1.40	1.35	0.000 ± 0.014	–	0.50 ± 0.02	–

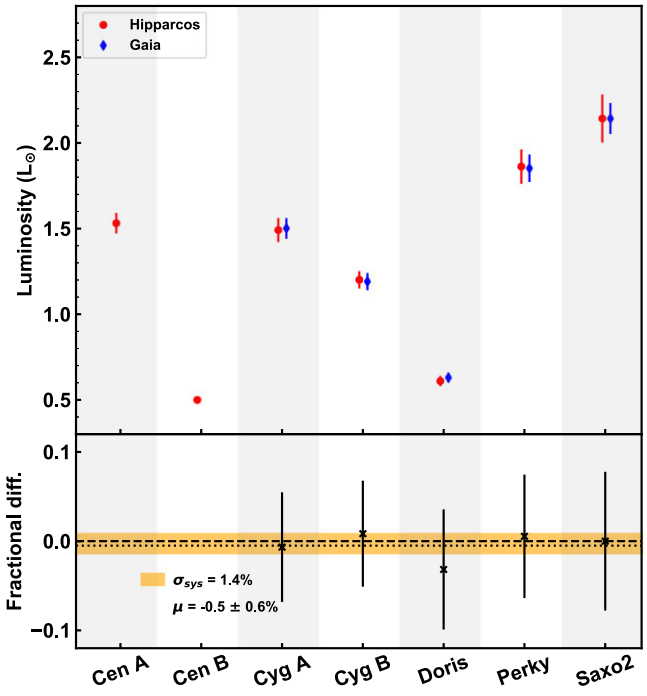

Figure 1. Top panel shows the comparison of the absolute parallax-based luminosities values and their corresponding uncertainties from *Hipparcos* (red circles) and *Gaia* (blue diamonds). The bottom panel shows the fractional difference in luminosity relative to the *Gaia*-based luminosity value, with a scatter of 1.4 per cent (orange colour), and an offset of -0.5 ± 0.6 per cent (dotted black line). No *Gaia* parallaxes are available for α Centauri A and B.

luminosities. This is because errors in $A_{\rm v}$ (determined based on equation 4) dominate the parallax errors during error propagation in equation (3).

Taking into account the *Gaia* parallaxes (shown in Table 2), and the angular diameter measurements of our benchmark stars (available from Huber et al. 2012b and White et al. 2013), we compute the interferometric radius measurements using the expression

$$R = \frac{1}{2}\theta_{\rm LD} D \,, \tag{5}$$

where $\theta_{\rm LD}$ is the angular diameter and D is the distance to the star, which is calculated directly from the parallax. The corresponding radius uncertainties were determined using the expression

$$\sigma(R) = R \times \sqrt{\left(\frac{\sigma(\theta_{\rm LD})}{\theta_{\rm LD}}\right)^2 + \left(\frac{\sigma(D)}{D}\right)^2} \,, \tag{6}$$

where $\sigma(\theta_{\rm LD})$ is the uncertainty on the angular diameter and $\sigma(D)$ is the uncertainty on the distance to the star.

2.4 Optimization process

In order to infer stellar parameters (mass and radius), we make use of the AIMS (Asteroseismic Inference on a Massive Scale; Rendle et al. 2019)[5] code, which relies on a pre-computed grid of models, and fits a specified set of atmospheric and seismic constraints using an MCMC (Markov Chain Monter Carlo; Gilks, Richardson & Spiegelhalter 1995; Gamerman 1998) approach. The advantage of the AIMS code over various seismic optimization codes is that it allows for interpolation within a pre-computed grid of models through tessellation/triangulation of the parameter space, thus enabling the identification of stellar evolutionary tracks located within the parameter space. Details are available in the AIMS documentation[6] and Rendle et al. (2019).

In a nutshell, AIMS allows for a generation of a subset of models which are representative of the specified constraints from which posterior distributions of the different model properties (such as mean density, radius, mass, age, among others) and their corresponding standard deviations, percentile ranges can be determined. The χ^2 is handled following the general expression

$$\chi^2 = \sum_{l=1}^{N} \left(\frac{A_i - B_i}{\sigma_i}\right)^2 \,, \tag{7}$$

where A_i, B_i, and σ_i are the observed parameters, model parameters, and corresponding associated observed uncertainties, respectively. The χ^2 in equation (7) is a composition of the seismic and atmospheric components expressed as

$$\chi^2 = \eta \left(\chi^2_{\rm seismic}\right) + \chi^2_{\rm atmospheric} \,, \tag{8}$$

where $\eta = N_a/N_\nu$, the ratio of the number of atmospheric constraints, N_a, to seismic constraints, N_ν. The inclusion of η in equation (8) facilities for the specification of equal weights, thus yielding the same weight for every observable in the likelihood function. It is important to note that depending on the approach adopted, the weights given to seismic and atmospheric constraints have an impact on the inferred stellar properties and their corresponding statistical uncertainties. Refer to Cunha et al. (2021) for an in-depth exploration of the impact of applying different weights on the derived stellar parameters arising from employing various model selection processes. The seismic χ^2 component in equation (8) makes use of the observed oscillation frequencies, $\nu_{\rm obs}$, their corresponding uncertainties, $\sigma(\nu)$, and the theoretical model oscillation frequencies, $\nu_{\rm mod}$, taking the form

$$\chi^2_{\rm seismic} = \sum_{l=1}^{N} \left(\frac{\nu^{\rm obs} - \nu^{\rm mod}}{\sigma(\nu)}\right)^2 \,. \tag{9}$$

[5] https://lesia.obspm.fr/perso/daniel-reese/spaceinn/aims/version2.0/
[6] https://sasp.gitlab.io/aims/

Table 3. Different combinations of seismic and atmospheric constraints.

Sets	observational combinations
1	[Fe/H], $T_{\rm eff}$, L
2	ν_i, [Fe/H], $T_{\rm eff}$
3	ν_i, [Fe/H], $T_{\rm eff}$, L

We note that the disparity between the observed oscillation frequencies and the model oscillation frequencies arising from the improper modelling of near-surface layers, also known as the 'surface effects' (Christensen-Dalsgaard, Dappen & Lebreton 1988; Dziembowski, Paterno & Ventura 1988; Christensen-Dalsgaard & Thompson 1997), was rectified using the two-term surface correction empirical formula suggested by Ball & Gizon (2014). A detailed comparison of the performance of different surface correction routines is given in Nsamba et al. (2018a), Compton et al. (2018), Jørgensen et al. (2020), among others. The atmospheric χ^2 component takes into account the available atmospheric contraints (i.e. effective temperature, $T_{\rm eff}$, metallicity, [Fe/H], luminosity, L) expressed as

$$\chi^2_{\rm atmospheric} = \chi^2_{T_{\rm eff}} + \chi^2_{\rm [Fe/H]} + \chi^2_{L}\,, \tag{10}$$

where $\chi^2_{T_{\rm eff}} = \left(\frac{T_{\rm eff}^{\rm (obs)} - T_{\rm eff}^{\rm (mod)}}{\sigma(T_{\rm eff})}\right)^2$, $\chi^2_{\rm [Fe/H]} = \left(\frac{T_{\rm eff}^{\rm (obs)} - T_{\rm eff}^{\rm (mod)}}{\sigma(T_{\rm eff})}\right)^2$, and $\chi^2_{L} = \left(\frac{L^{\rm (obs)} - L^{\rm (mod)}}{\sigma(L)}\right)^2$. In cases where an interferometric radius is available, we assess its contribution towards the determination of a precise stellar mass by replacing the $\chi^2_{\rm L}$ in equation (10) with the radius χ^2 which takes the form $\chi^2_{R} = \left(\frac{R^{\rm (obs)} - R^{\rm (mod)}}{\sigma(R)}\right)^2$. The superscripts 'obs' and 'mod' in the definitions of the respective χ^2 terms of equation (10) correspond to the observed and model parameters.

The scatter (systematic uncertainties, $\sigma_{\rm sys}$) on the inferred stellar parameters were determined using the expression

$$\sigma_{\rm sys} = \sqrt{\frac{1}{N}\left(\sum_i (x_i - \mu)^2\right)}\,, \tag{11}$$

where N corresponds to the total number of quantities while x_i denotes the fractional differences between quantities. The mean (offset, μ) and it's corresponding error (σ_μ) are obtained using the expression

$$\mu = \sum \frac{x_i}{N} \tag{12}$$

and

$$\sigma_\mu = \frac{\sigma_{\rm sys}}{\sqrt{N}}\,, \tag{13}$$

respectively. This aids in establishing the accuracy level of the inferred parameters.

3 RESULTS AND DISCUSSIONS

3.1 Impact of a stellar luminosity on the inferred radius and mass

Table 3 shows a combination of different atmospheric and seismic constraints used in establishing the relevance of a stellar luminosity towards the determination of stellar radius and mass. The top panel of Fig. 2 and Table 4 show that the inferred stellar radii from Set 1 yields the least precise values compared to Set 2 and Set 3. This is because constraints in Set 1 allow for a combination of an effective temperature and luminosity via the Stefan–Boltzmann's relation (Boltzmann 1884; Paul et al. 2015; Montambaux 2018), thus placing a restriction on the model radius selection process and consequently the mass. Set 2 and Set 3 include seismic data as an additional constraint, provided via individual oscillation frequencies in the optimization process, putting strong restriction on the stellar mean density and radius. Similar findings were reached in terms of precision of the inferred masses (see top panel of Fig. 3; black circle symbols and Table 5), except for α Centauri A and B. This stems from the ground-based seismic data (for α Centauri A and B) which

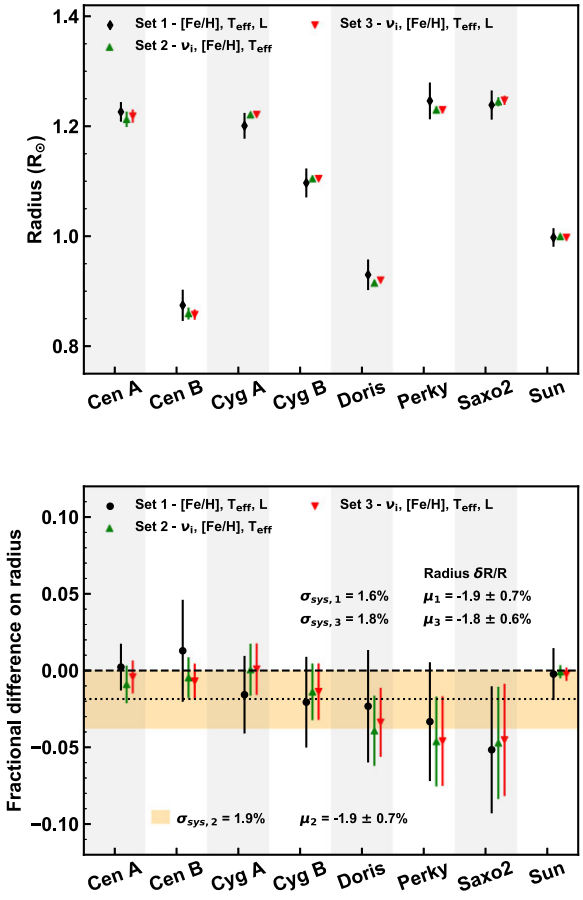

Figure 2. Top panel: comparison of the derived absolute radii and their associated uncertainties from different observable combinations. Bottom panel: fractional difference in radius relative to the interferometric radius. Orange colour and dotted black line display the scatter ($\sigma_{sys,2}$) and an offset (μ_2) based on Set 2, respectively. For comparison purposes, the values for the scatter and offset based on Set 1 and Set 3 are also included.

Table 4. Inferred stellar radii from the different observable combinations. For the definition of included observables in each set, see Table 3.

Star	Set 1	Set 2	Set 3
Cyg A	1.201 ± 0.023	1.221 ± 0.005	1.221 ± 0.004
Cyg B	1.097 ± 0.026	1.104 ± 0.005	1.105 ± 0.005
Doris	0.929 ± 0.028	0.915 ± 0.006	0.920 ± 0.004
Perky	1.246 ± 0.033	1.229 ± 0.007	1.230 ± 0.007
Saxo2	1.239 ± 0.027	1.244 ± 0.008	1.247 ± 0.008
Cen A	1.226 ± 0.018	1.212 ± 0.014	1.218 ± 0.012
Cen B	0.874 ± 0.028	0.859 ± 0.011	0.857 ± 0.009
Sun	0.998 ± 0.004	0.999 ± 0.004	0.998 ± 0.004

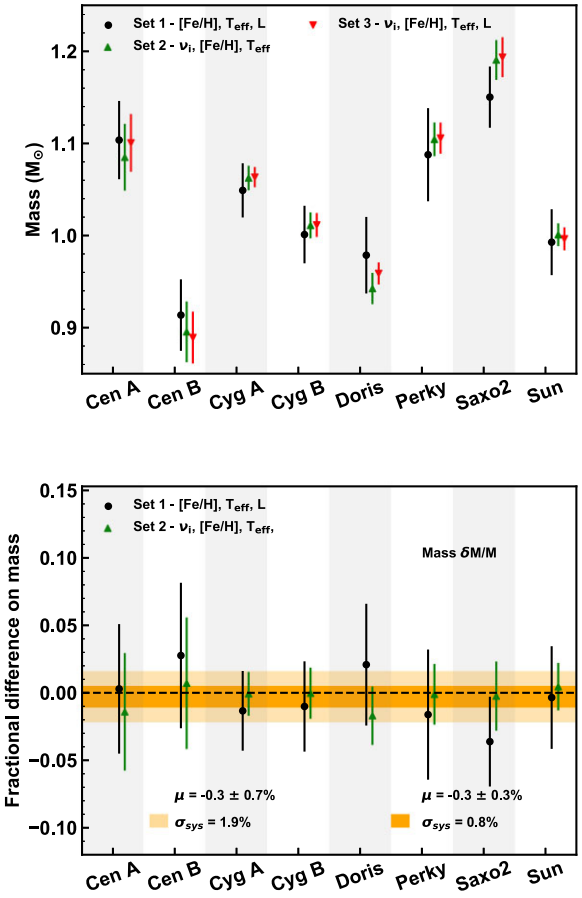

Figure 3. Top panel: comparison of the derived absolute masses and their associated uncertainties from different observable combinations. Bottom panel: fractional difference in mass derived using other Sets relative to Set 3. Light orange colour shows the scatter (systematics) and corresponding offset (bias) when Set 1 is compared with Set 3, while the dark orange colour compares Set 2 and Set 3.

is not as precise as the *Kepler* space based seismic data used for the remaining sample of our benchmark stars (Carrier & Bourban 2003; Meulenaer et al. 2010; Lund et al. 2017). Furthermore, the mass and radius probability distributions become slightly more narrow as the constraints where changed from Sets 2 to 3 (see left and right panels of Fig. 4). The combinations of observables in Sets 3 produce higher mass and radius probabilities followed by Set 2. This demonstrates that the addition of a parallax-based luminosity contributes vital information in finding the most probable stellar parameter.

The bottom panel of Fig. 2 highlights that the inferred stellar radii for majority of our stellar sample are underestimated compared to their interferometric radii values, yielding an offset of up-to -1.9 ± 0.7 per cent and a scatter of $\sim$1.9 per cent. We note that this scatter relatively reduces for combinations involving luminosity as an additional constraint, i.e. $\sim$1.6 per cent and $\sim$1.8 per cent for Set 1 and Set 2, respectively. Since no independent stellar masses are available for our binary stars, except for α Centauri A and B, we considered the inferred masses from Set 3 as a reference in the bottom panel of Fig. 3. Our findings show that when the masses from Set 1 (only atmospheric constraints) are compared with those from Set 2 (commonly used combination of seismic and classical constraints), and Set 2 compared with Set 3 (includes a stellar luminosity), an offset of -0.3 per cent is attained, while the scatter is reduced from 1.9 per cent to 0.8 per cent, respectively.

3.2 Impact of a model-independent radius on the inferred mass

Table 6 shows a combination of constraints used in examining the accuracy and precision of inferred masses when an interferometric radius is adopted instead of a stellar luminosity. The top and bottom panels of Fig. 5 show that the precision of the derived stellar masses improves when observable combinations are varied from Set 4 to Set 5, yielding a scatter of 3 per cent and an offset of -1.1 ± 0.9 per cent. It is also evident that the masses obtained using Set 4 are underestimated compared to those from Set 5 (See bottom panel of Fig. 5). It is important to note that Set 5 includes seismic data via the individual oscillation frequencies which places strong constraints on the stellar mean density, and with a known radius, the mass is indirectly constrained, while Set 4 does not place any constraints on the stellar mass.

Next, we assess how the precision of a model-independent radius (interferometric radius) impacts on the determination of a robust stellar mass. We consider α Centauri A as a reference star for this exercise. α Centauri A has both an interferometric radius and a dynamical mass with associated errors below 1percnt, i.e. $R_{\rm A} = 1.2234 \pm 0.0053\,{\rm R}_{\odot}$ and $M_{\rm A} = 1.1055 \pm 0.004\,{\rm M}_{\odot}$, respectively (Kervella et al. 2017). We perform the best-fitting model selection process by considering constraints in Set 5. The error on the interferometric radius was varied from 1σ to 7σ. For each combination, a mass is derived. The top panel of Fig. 6 highlights the trend of how the uncertainty on the inferred stellar mass varies with the uncertainty on the interferometric radius. For an interferometric radius with the uncertainty of $\lesssim$1 per cent, the uncertainties on the inferred masses are $\lesssim$2.5 per cent. In addition, an interferometric radius with the uncertainty of 0.5 per cent yields a corresponding uncertainty of about 1.5 per cent on stellar mass. It is worth noting that the uncertainty on the inferred mass increases as that on the interferometric radius

Table 5. Inferred stellar masses from the different observable combinations.

Star	Set 1	Set 2	Set 3	Set 4	Set 5
Cyg A	1.05 ± 0.03	1.06 ± 0.01	1.06 ± 0.01	1.04 ± 0.03	1.06 ± 0.01
Cyg B	1.00 ± 0.03	1.01 ± 0.01	1.01 ± 0.01	0.98 ± 0.03	1.01 ± 0.01
Doris	0.98 ± 0.04	0.94 ± 0.02	0.96 ± 0.01	0.96 ± 0.06	0.97 ± 0.01
Perky	1.09 ± 0.05	1.10 ± 0.02	1.11 ± 0.02	1.07 ± 0.05	1.11 ± 0.02
Saxo2	1.15 ± 0.03	1.19 ± 0.02	1.19 ± 0.02	1.15 ± 0.03	1.19 ± 0.02
Cen A	1.10 ± 0.04	1.08 ± 0.04	1.10 ± 0.03	1.11 ± 0.04	1.08 ± 0.03
Cen B	0.91 ± 0.03	0.89 ± 0.03	0.89 ± 0.03	0.91 ± 0.04	0.90 ± 0.03
Sun	0.99 ± 0.03	1.00 ± 0.01	1.00 ± 0.01	0.99 ± 0.03	1.00 ± 0.001

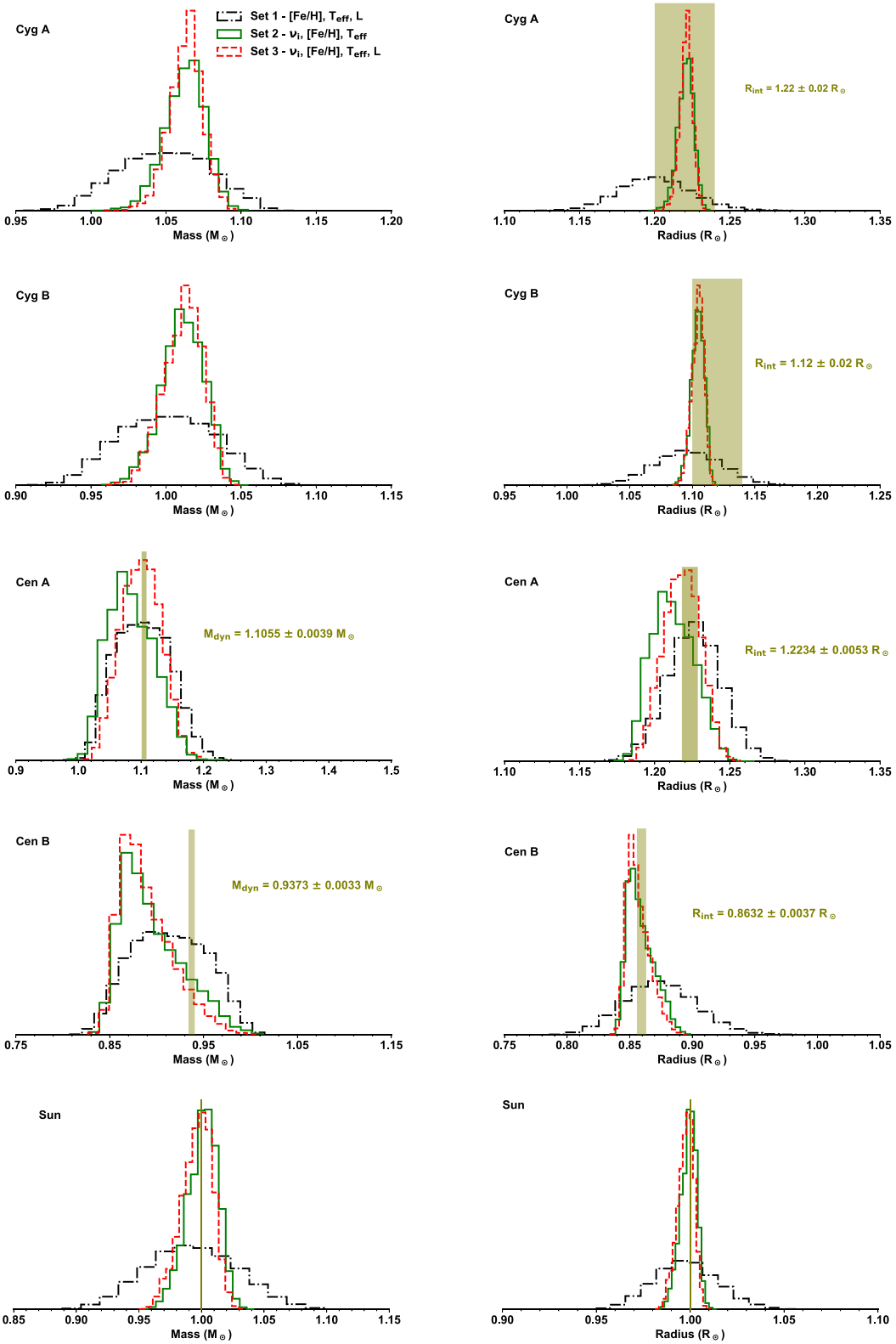

Figure 4. Normalized probability density distributions for mass (left panels) and radius (right panels). Colour-code and line style shows results obtained using different observable combinations, i.e. Set 1 (black dash–dotted line), Set 2 (green line), and Set 3 (red dashed line). The olive region given in some cases refers to independent values of radius and mass, if available.

Table 6. Different combinations of seismic and atmospheric constraints.

Sets	observational combinations
4	[Fe/H], $T_{\rm eff}$, R
5	ν_i, [Fe/H], $T_{\rm eff}$, R

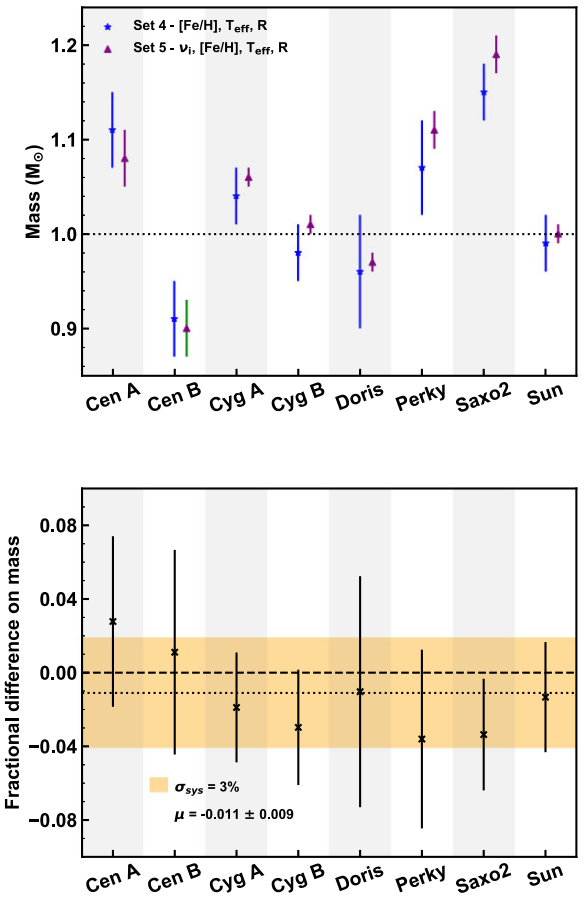

Figure 5. Top panel: comparison of the derived absolute masses and their associated uncertainties from different observable combinations with an interferometric radii taken into account in the optimization process. Bottom panel: fractional difference in mass derived from Set 4 relative to Set 5. Light orange colour shows the scatter (systematics) while the dotted black line shows an offset.

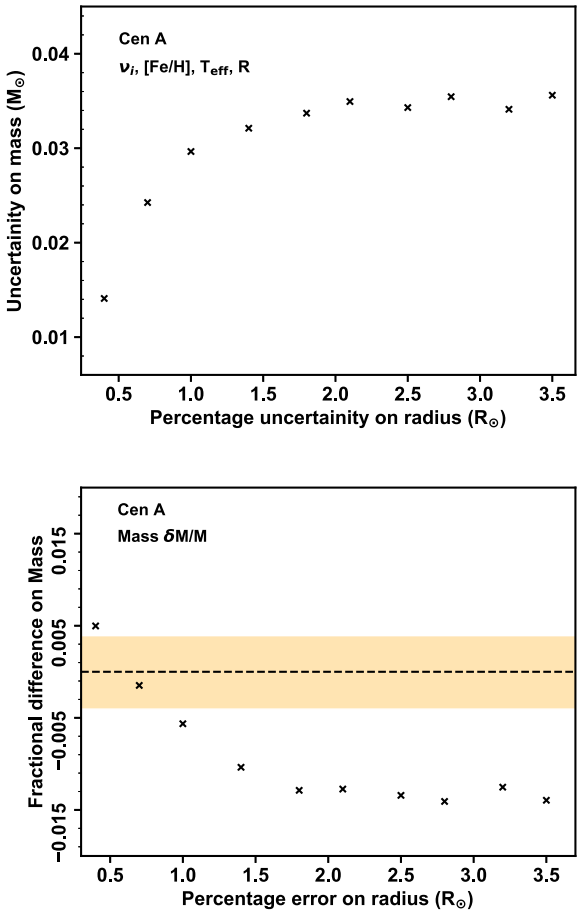

Figure 6. Statistical uncertainties (top panel) and fractional differences between the inferred masses and dynamical mass of α Centauri A (bottom panel) against the varied uncertainties on interferometric radius. The orange region represents the dynamical mass range. The error on the interferometric radius was varied from 1σ ($\sim$0.5 per cent) to 7σ ($\sim$3.5 per cent).

increases, and becomes relatively constant when the uncertainty on the interferometric radius is above $\sim$1.5 per cent (see top panel of Fig. 6). At this level, the interferometric radius is no longer restrictive, and the total mass uncertainty is determined by all the other measured quantities.

The bottom panel of Fig. 6 shows that the stellar mass is accurately determined when an interferometric radius with a precision below $\sim$1 per cent is used in the optimization process. A model-independent radius at this level of precision dominates the seismic data in the determination of a stellar mass. The impact of the interferometric radius vanishes once its uncertainty is above $\sim$1.5 per cent. This is because the seismic observables (individual oscillation frequencies) dominate other specified observables (including a non-precise interferometric radius) towards the determination of the stellar mass. Our findings are consistent with predictions based on theoretical simulations by Creevey et al. (2007). Based on these findings, in order to mitigate a scatter of about $\sim$5percnt on the inferred asteroseismic stellar mass arising from variations in model physics and/or optimization tool employed (e.g Silva Aguirre et al. 2015, 2017; Nsamba et al. 2018a), it would be vital to include an interferometric radius if available, among the observable constraints. However, we note that this is only relevant if the precision on the interferometric radius is about $\lesssim$1 per cent.

3.3 Influence of the quality and length of seismic data on the inferred masses and radii.

We examine how seismic data, when complemented with atmospheric constraints (effective temperature, metallicity, and luminosity), perform towards yielding robust stellar masses and radii. This analysis is based on two stars, i.e 16 Cyg A with high signal to noise observations from *Kepler* available (Lund et al. 2017) and α Centauri A observed with ground-based observations, yielding oscillation frequencies with relatively low precision (Meulenaer et al. 2010).We perform different runs for both 16 Cyg A and α Centauri A fitting different seismic modes, i.e. all $l = 0$ modes, $l = 0, 1$ modes, $l = 0, 1, 2$ modes, and $l = 0, 1, 2, 3$ modes, complemented with atmospheric constraints. The top panels of Fig. 7 show that when the spherical degree modes are increased from $l = 0$ to $l = 0, 1, 2$ modes, the number of acceptable models reduces yielding more narrower probability distributions, thus demonstrating

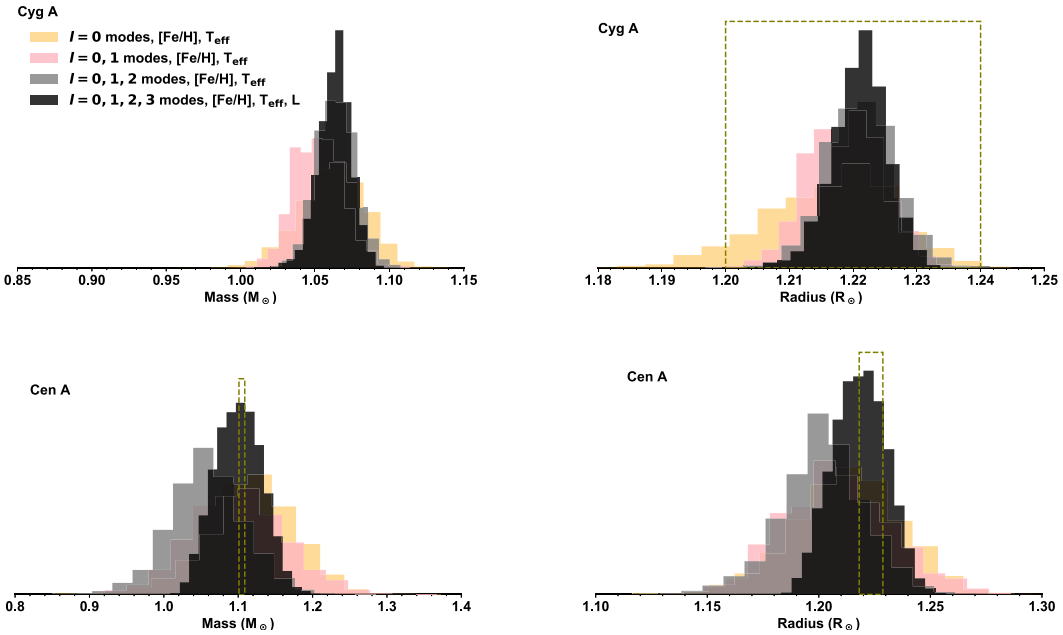

Figure 7. Normalized probability density distributions for mass (left panels) and radius (right panels) of 16 Cyg A (top panels) and α Centauri A (bottom panels). Colour-coded according to the applied oscillation frequency modes and atmospheric constraints. The dashed olive lines correspond to independent radii and masses.

that more seismic information yields better constrained masses and radii measurements. In addition, the top right panel of Fig. 7 shows that the inferred radii from the different modes of 16 Cyg A are also in excellent agreement with the interferometric radius. The bottom panels of Fig. 7 show that the optimal masses and radii of α Centauri A, inferred when $l = 0$ modes and $l = 0, 1$ modes are used in the optimization process, are in good agreement with the dynamical mass and interferometric radius, respectively. However, an offset in the derived mass and radius can be observed when modes of $l = 0, 1, 2$ are used. This could partly stem from the available ground-based seismic data of α Centauri A, which are less precise. Complementing this seismic data with $l = 3$ modes and atmospheric constraints with a *Gaia*-based luminosity, yields the optimal inferred mass and radius which are in good agreement with the dynamical mass and interferometric radius.

In Fig. 8, we explore the impact of varying the number of $l = 0$ mode oscillation frequencies (i.e. from 4, 8, and 12 frequencies) on the inferred mass and radius. The top right panel of Fig. 8 shows that inferred radii of 16 Cyg A obtained when the number of $l = 0$ mode oscillation frequencies is varied are in good agreement with the interferometric radius. However, as the number of oscillation frequencies is increased (from 4, 8, and 12 frequencies), the number of acceptable models is reduced and narrower probability distributions are obtained. The top right panel of Fig. 8 also shows that consistent probability distributions are obtained when 12 oscillation frequencies of $l = 0$ mode and all $l = 0, 1, 2, 3$ mode frequencies are used in the optimization process, with the latter yielding a higher radius probability. Similar findings are obtained for the mass of 16 Cyg A (see top left panel of Fig. 8). Unfortunately, no model-independent mass is available for this star, thus we ascertain the accuracy of the inferred masses by considering the case of α Centauri A. When the number of $l = 0$ mode oscillation frequencies is increased (from 4 to 8 and 12 frequencies), their dominance also increases over the atmospheric constraints (effective temperature, metallicity, and luminosity), leading to a more constrained/narrower probability distributions of both radius and mass (see top panels of Fig. 8). The bottom panels of Fig. 8 show that the probability distributions of both mass (left bottom panel) and radius (right bottom panel) produced from the different $l = 0$ mode oscillation frequencies are relatively consistent. This is because the seismic observations of α Centauri A are ground-based and not as precise as space observations (case of 16 Cyg A). Thus, little additional information is obtained from increasing the number of less precise $l = 0$ mode oscillation frequencies which could play a significant role in further restricting the model selection process. From the bottom panels of Fig. 8, the inferred masses and radii from all the different distributions are in agreement within the uncertainties with the dynamical mass and interferometric radius, respectively. In general and based on the panels of Fig. 8, the precision and number of $l = 0$ mode oscillation frequencies play a vital role towards the determination of robust masses and radii in forward modelling processes.

Although this article focuses mainly on the inferred masses and radii, we briefly highlight the impact of the length and quality of seismic data on the inferred ages. We note that stellar ages inferred through asteroseismic forward modelling procedures are highly model-dependent and significantly vary depending on the model physics specified (e.g. Silva Aguirre et al. 2015, 2017; Nsamba et al. 2018a). Since no independent ages are available, our reference ages are based on those inferred using Set 3 (see Table 3, i.e. from a combination of all individual oscillation frequencies of $l = 0, 1, 2, 3$ modes, effective temperature, metallicity, and parallax-based luminosity). We again consider 16 Cyg A and α Centauri A because of the difference in the quality of the available seismic data. Fig. 9 shows that the probability distributions for both 16 Cyg A and α Centauri A span a wide range of values when only $l = 0$ modes (orange) and $l = 0, 1$ modes (pink) are employed. This demonstrates that no strong constraint is placed on the age parameter. However, a reduced age parameter range (narrow

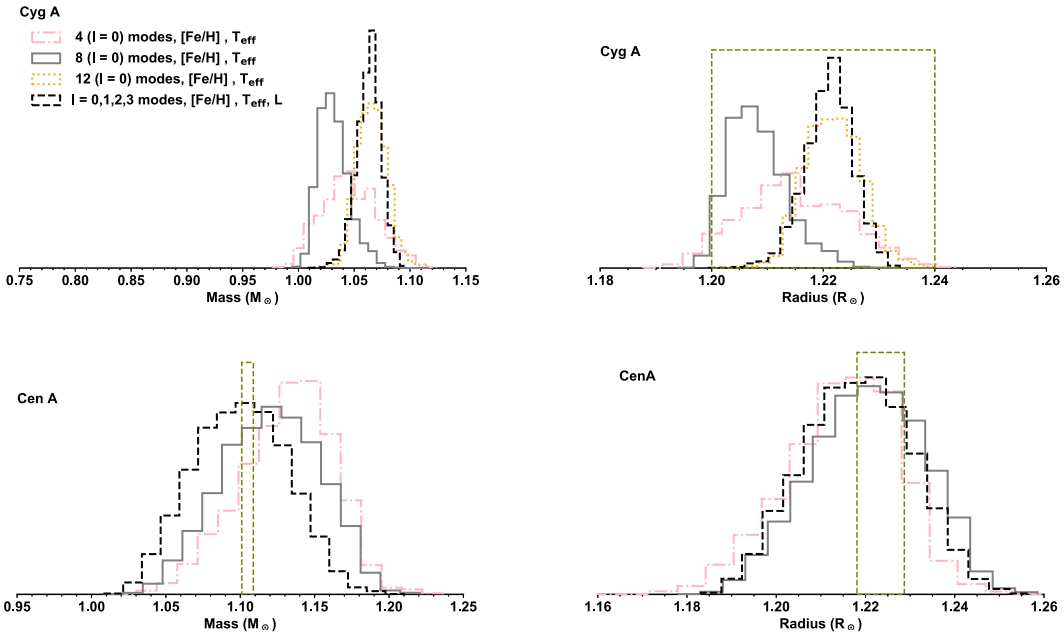

Figure 8. Normalized probability density distributions for mass (left panels) and radius (right panels) of 16 Cyg A (top panels) and α Centauri A (bottom panels). Colour-code according to the number of frequency modes: Pink dashed–dotted line – 4 ($l = 0$) modes, Grey dashed line – 8 ($l = 0$) modes, Orange dotted line – 12 ($l = 0$) modes, and black dashed line – all ($l = 0, 1, 2, 3$) modes. The dashed olive lines correspond to independent radii and masses.

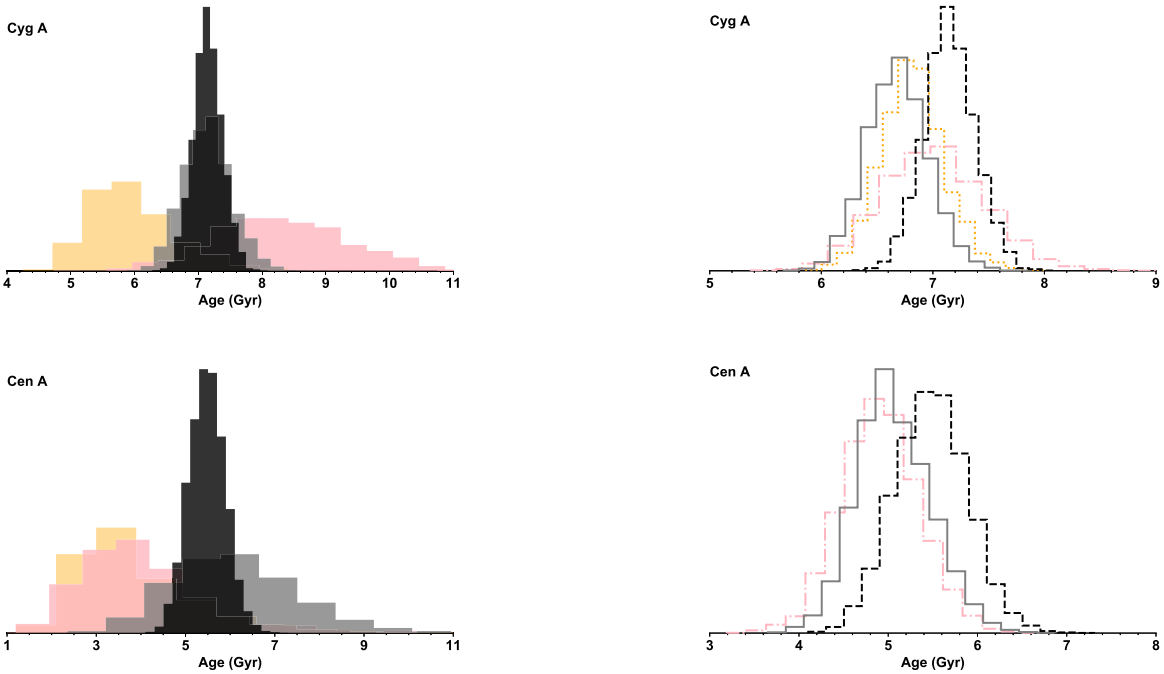

Figure 9. Same as Fig. 7, but for stellar age.

Figure 10. Same as Fig. 8 but for stellar age.

probability distributions) is generated when $l = 0, 1, 2$ modes are used. An excellent agreement can be seen in the top panel of Fig. 9 when probability distributions obtained using $l = 0, 1, 2$ modes (grey) are compared with those obtained using constraints of Set 4 (black). The bottom panel of Fig. 9 shows that although $l = 0, 1, 2$ modes and constraints in Set 4 yield consistent mean age value of α Centauri A, the probability distributions are not as narrow as in the case of 16 Cyg A (top panel of Fig. 9). This may be attributed to the difference in the precision of the available seismic data (i.e. ground-based data for the case of α Centauri A). Fig. 10 shows that the consistent ages (agreement within 1σ) are obtained when the number of individual frequencies of only $l = 0$ modes are varied (i.e. from 4, 8, and 12 frequencies). The top and bottom panels of Fig. 10 show that increasing the number of $l = 0$ modes frequencies from 4 to 8 leads to a higher age probability. No significant difference is observed when the number of $l = 0$ modes frequencies is increased from 8 to 12. We note that only 10 ($l = 0$ modes) frequencies

are available for α Centauri A, this explains why no probability distribution (orange) is shown in the bottom panel of Fig. 10.

4 SUMMARY AND CONCLUSIONS

In this article, we made use of a sample of main-sequence benchmark stars and explored the influence of a parallax-based luminosity when combined with other observational constraints (both seismic and atmospheric) towards improving the precision and accuracy of stellar mass and radius. Our selected stellar sample have model-independent radii available (interferometric radii), thus aiding to ascertaining not only the precision but also the accuracy of the derived radius parameters when considering different observational constraint combinations. Further, three stars in our stellar sample have model-independent masses allowing us to validate the accuracy of the inferred masses. In addition, we have explored the precision needed on a model-independent radius if it is to have a vital influence in the determination of a precise mass. Lastly, we explored how the quality and length of seismic data affect the robustness of inferred stellar masses and radii. Despite the fact that stellar ages are highly model-dependent, we briefly highlight the impact of the quality and length of seismic data on the inferred ages. A comprehensive complementary study on stellar ages is presented in Kamulali et al. (in preperation).

The precision of the inferred stellar mass improves when seismic and spectroscopic constraints (effective temperature and metallicity) are complemented with a *Gaia*-based luminosity, i.e. with a scatter varying from 1.9 per cent to 0.8 per cent. However, the inferred stellar radius is underestimated when compared to the interferometric radius, with an offset of -1.9 ± 0.7 per cent and a scatter of up to 1.9 per cent. Our findings also demonstrate that an independent radius with a precision below 1 per cent when applied in the optimization process yields a mass with a precision below 1.5 per cent. This may hold the key in overcoming systematic uncertainties (scatter) induced on the inferred stellar mass arising from the improper description and modelling of stellar physics. Thus, these results recommend for an improvement in the interferometric measurements so at to reach a precision of $\sim$1 per cent in interferometric radius of solar-type stars, needed to infer robust masses.

The results of this article also show that in cases where oscillation frequencies of higher degree modes (i.e. $l \gtrsim 1$, 2 and 3) are not available, robust masses and radii can still be attained with precise $l = 0$ mode oscillations frequencies coupled with atmospheric constraints. However, the precision of the inferred masses and radii can be significantly improved when numerous precise $l = 0$ mode oscillations frequencies (>8) are taken into account. Our results also highlight that it is essential to complement non-precise seismic data (ground-based) with atmospheric constraints (including a *Gaia*-based luminosity) if robust masses and radii are to be derived. We also note that individual oscillation frequencies of at least $l = 0$, 1, 2 modes need to be taken into account in the forward modelling process if constrained age probability distributions are to be obtained, fewer modes result to the age probability distributions spanning a wide range of values.

This article demonstrates the relevance of *Gaia*-based parallax measurements when complemented with other observational constraints in improving the precision and accuracy of inferred stellar masses and radii. The findings in this article should be taken into account in PLATO work packages related to the characterization of stellar properties. Furthermore, an extended stellar sample with model-independent masses (dynamical masses) and with high-quality seismic data made available from the PLATO mission will offer an opportunity to extensively examine the accuracy of masses derived through forward modelling, and the contribution of a stellar luminosity in yielding more accurate masses.

ACKNOWLEDGEMENTS

The authors acknowledge the anonymous referee for the helpful and constructive remarks, which helped to significantly improve this paper. BN acknowledges postdoctoral funding from the 'Branco Weiss fellowship – Science in Society' through the SEISMIC stellar interior physics group. JK acknowledges funding through the Max-Planck Partnership group – SEISMIC Max-Planck-Institut für Astrophysik (MPA) – Germany and Kyambogo University (KyU) – Uganda. We also acknowledge funding from the UNESCO-TWAS programme, 'Seed Grant for African Principal Investigators' financed by the German Ministry of Education and Research (BMBF). BN thanks Nuno Moedas for providing evolution models for comparisons, Dr Margarida S. Cunha and Dr Savannah Nuwagaba for the useful discussions.

DATA AVAILABILITY

Stellar model data generated in this article using the stellar evolution code (MESA) will be made available on request. The MESA 'inlists' describing the stellar physics highlighted in Section 2.1 will be provided. The oscillation frequencies data used for our sample stars are available in Lund et al. (2017).

REFERENCES

Ahlborn F., Kupka F., Weiss A., Flaskamp M., 2022, A&A, 667, A97
Akeson R., Beichman C., Kervella P., Fomalont E., Benedict G. F., 2021, AJ, 162, 14
Angulo C. et al., 1999, Nucl. Phys. A, 656, 3
Asplund M., Grevesse N., Sauval A. J., Scott P., 2009, ARA&A, 47, 481
Auvergne M. et al., 2009, A&A, 506, 411
Ball W. H., Gizon L., 2014, A&A, 568, A123
Basu S., Kinnane A., 2018, ApJ, 869, 8
Bazot M., Bourguignon S., Christensen-Dalsgaard J., 2012, MNRAS, 427, 1847
Bazot M., Christensen-Dalsgaard J., Gizon L., Benomar O., 2016, MNRAS, 460, 1254
Beck P. G. et al., 2023, A&A, 682, 27
Bedding T. R., Kjeldsen H., Butler R. P., McCarthy C., Marcy G. W., O'Toole S. J., Tinney C. G., Wright J. T., 2004, ApJ, 614, 380
Bedding T. R. et al., 2005, A&A, 432, L43
Bellinger E. P., Basu S., Hekker S., Ball W. H., 2017, ApJ, 851, 80
Benomar O., Masuda K., Shibahashi H., Suto Y., 2014, PASJ, 66, 21
Boltzmann L., 1884, Annalen der Physik, 258, 291
Borucki W. J. et al., 2010, Science, 327, 977
Bouchy F., Carrier F., 2002, A&A, 390, 205
Buchhave L. A., Latham D. W., 2015, ApJ, 808, 187
Campante T. L. et al., 2016, ApJ, 819, 85
Campante T. L. et al., 2019, ApJ, 885, 12
Capitanio L., Lallement R., Vergely J. L., Elyajouri M., Monreal-Ibero A., 2017, A&A, 606, A65
Carrier F., Bourban G., 2003, A&A, 406, L23
Christensen-Dalsgaard J., Thompson M. J., 1997, MNRAS, 284, 527
Christensen-Dalsgaard J., Dappen W., Lebreton Y., 1988, Nature, 336, 634
Cochran W. D., Hatzes A. P., Butler R. P., Marcy G. W., 1997, ApJ, 483, 457
Compton D. L., Bedding T. R., Ball W. H., Stello D., Huber D., White T. R., Kjeldsen H., 2018, MNRAS, 479, 4416
Cox J. P., Giuli R. T., 1968, Principles of stellar structure. Gordon and Breach, New York
Creevey O. L., Monteiro M. J. P. F. G., Metcalfe T. S., Brown T. M., Jiménez-Reyes S. J., Belmonte J. A., 2007, ApJ, 659, 616

Creevey O. L. et al., 2012, A&A, 545, A17
Creevey O. L. et al., 2015, A&A, 575, A26
Cunha M. S. et al., 2021, MNRAS, 508, 5864
Cyburt R. H., Fields B. D., Olive K. A., 2003, Phys. Lett. B, 567, 227https://doi.org/10.1016/j.physletb.2003.06.026
Davies G. R. et al., 2015, MNRAS, 456, 2183
Deal M., Alecian G., Lebreton Y., Goupil M. J., Marques J. P., LeBlanc F., Morel P., Pichon B., 2018, A&A, 618, A10
Deal M., Goupil M. J., Marques J. P., Reese D. R., Lebreton Y., 2020, A&A, 633, A23
de Meulenaer P., Carrier F., Miglio A., Bedding T. R., Campante T. L., Eggenberger P., Kjeldsen H., Montalbán J., 2010, A&A, 523, A54
Döner S., Ak S., Önal Taş Ö., Plevne O., 2023, Phys. Astron. Rep., 1, 11
Doğan G. et al., 2013, ApJ, 763, 49
Dziembowski W. A., Paterno L., Ventura R., 1988, A&A, 200, 213
Eggenberger P., Charbonnel C., Talon S., Meynet G., Maeder A., Carrier F., Bourban G., 2004, A&A, 417, 235
Farnir M., Dupret M. A., Buldgen G., Salmon S. J. A. J., Noels A., Pinçon C., Pezzotti C., Eggenberger P., 2020, A&A, 644, A37
Ferguson J. W., Alexander D. R., Allard F., Barman T., Bodnarik J. G., Hauschildt P. H., Heffner-Wong A., Tamanai A., 2005, ApJ, 623, 585
Fitzpatrick E. L., 1999, PASP, 111, 63
Flower P. J., 1996, ApJ, 469, 355
Gaia Collaboration et al., 2018, A&A, 616, A1
Gaia Collaboration et al., 2023, A&A, 674, A1
Gamerman D., 1998, Biometrika, 85, 215
Gilks W., Richardson S., Spiegelhalter D., 1995, Chapman and Hall/CRC, 512
Gilliland R. L. et al., 2010, PASP, 122, 131
Guo Z., Jiang C., 2023, Astron. Comput., 42, 100686
Halbwachs J. L. et al., 2020, MNRAS, 496, 1355
Hauser H. M., Marcy G. W., 1999, PASP, 111, 321
Herwig F., 2000, A&A, 360, 952
Huber D., Stello D., Bedding T. R., Chaplin W. J., Arentoft T., Quirion P.-O., Kjeldsen H., 2009, Commun. Asteroseismology, 160, 74
Huber D. et al., 2012a, MNRAS, 423, L16
Huber D. et al., 2012b, ApJ, 760, 32
Huber D. et al., 2017, ApJ, 844, 102
Huber D. et al., 2019, AJ, 157, 245
Huebner W. F., Barfield W. D., 2014, Equations of State and Opacities for Mixtures. Springer New York, New York, NY, p. 405, https://doi.org/10.1007/978-1-4614-8797-5_10
Iglesias C. A., Rogers F. J., 1996, ApJ, 464, 943
Imbriani G. et al., 2005, EPJ A, 25, 455
Ireland M. J. et al., 2008, in Schöller M., Danchi W. C., Delplancke F., eds, Proc. SPIE Conf. Ser. Vol. 7013, Optical and Infrared Interferometry. SPIE, Bellingham, p. 701324
Jiang C. et al., 2020, ApJ, 896, 65
Jørgensen A. C. S. et al., 2020, MNRAS, 495, 4965
Joyce M., Chaboyer B., 2018, ApJ, 864, 99
Karoff C. et al., 2018, ApJ, 852, 46
Karovicova I., White T. R., Nordlander T., Casagrand e L., Ireland M., Huber D., Jofré P., 2020, A&A, 640, 12
Kervella P., Thévenin F., Ségransan D., Berthomieu G., Lopez B., Morel P., Provost J., 2003, A&A, 404, 1087
Kervella P., Mignard F., Mérand A., Thévenin F., 2016, A&A, 594, A107
Kervella P., Bigot L., Gallenne A., Thévenin F., 2017, A&A, 597, A137
Kiefer R., Broomhall A.-M., 2020, MNRAS, 496, 4593
Kiefer R., Schad A., Davies G., Roth M., 2017, A&A, 598, A77
Kjeldsen H., Bedding T. R., 2004, in Danesy D., ed., ESA Special Publication Vol. 559, SOHO 14 Helio- and Asteroseismology: Towards a Golden Future. p. 101
Kjeldsen H., Bedding T. R., 2005, Highlights Astron., 13, 407
Kjeldsen H. et al., 2005, ApJ, 635, 1281
Krishna Swamy K. S., 1966, ApJ, 145, 174
Lallement R., Vergely J. L., Valette B., Puspitarini L., Eyer L., Casagrande L., 2014, A&A, 561, A91
Lebreton Y., Goupil M. J., Montalbán J., 2014, in Lebreton Y., Valls-Gabaud D., Charbonnel C., eds, EAS Pub. Ser. Vol. 65, EAS Publications Series. p. 177
Ligi R. et al., 2016, A&A, 586, A94
Lund M. N. et al., 2017, ApJ, 835, 172
Lundkvist M. S. et al., 2016, Nature Commun., 7, 11201
Mathur S. et al., 2012, ApJ, 749, 152
Mazumdar A. et al., 2009, A&A, 503, 521
Meftah M. et al., 2018, A&A, 616, A64
Metcalfe T. S., Charbonneau P., 2003, J. Comput. Phys., 185, 176
Metcalfe T. S. et al., 2010, ApJ, 723, 1583
Metcalfe T. S. et al., 2012, ApJL, 748, L10
Metcalfe T. S. et al., 2014, ApJS, 214, 27
Metcalfe T., Townsend R., Ball W., 2023, Res. Notes AAS, 7 164
Miglio A., Montalbán J., 2005, A&A, 441, 615
Miglio A. et al., 2017, Astron. Nachr., 338, 644
Moedas N., Nsamba B., Clara M. T., 2020, in Monteiro Mário J. P. F. G., García Rafael A., Christensen-Dalsgaard Jørgen, McIntosh Scott W., eds, Astrophys. Space Sci. Lib. Vol. 57, Dynamics of the Sun and Stars; Honoring the Life and Work of Michael J. Thompson. Springer International Publishing, p. 259
Moedas N., Deal M., Bossini D., Campilho B., 2022, A&A, 666, A43
Montambaux G., 2018, Found. Phys., 48, 395
Monteiro M. J. P. F. G., 2009, Evolution and Seismic Tools for Stellar Astrophysics. Vol. 316
Nielsen M. B. et al., 2020, A&A, 641, 11
Nsamba B., Campante T. L., Monteiro M. J. P. F. G., Cunha M. S., Rendle B. M., Reese D. R., Verma K., 2018a, MNRAS, 477, 5052
Nsamba B., Monteiro M. J. P. F. G., Campante T. L., Cunha M. S., Sousa S. G., 2018b, MNRAS, 479, L55
Nsamba B., Campante T. L., Monteiro M. J. P. F. G., Cunha M. S., Sousa S. G., 2019, Front. Astron. Space Sci., 6, 25
Nsamba B. et al., 2021, MNRAS, 500, 54
Nsamba B., Cunha M. S., Rocha C. I. S. A., Pereira C. J. G. N., Monteiro M. J. P. F. G., Campante T. L., 2022, MNRAS, 514, 893
Paul H., Greenberger D. M., Stenholm S. T., Schleich W. P., 2015, Phys. Scripta Volume T, T165, 014027
Paxton B., Bildsten L., Dotter A., Herwig F., Lesaffre P., Timmes F., 2011, ApJS, 192, 3
Paxton B. et al., 2013, ApJS, 208, 4
Paxton B. et al., 2015, ApJS, 220, 15
Paxton B. et al., 2018, ApJS, 234, 34
Paxton B. et al., 2019, ApJS, 243, 10
Pijpers F. P., 2003, A&A, 400, 241
Pourbaix D., Boffin H. M. J., 2016, A&A, 586, A90
Prša A. et al., 2016, AJ, 152, 41
Ramírez I., Meléndez J., Asplund M., 2009, A&A, 508, L17
Rauer H. et al., 2014, Exp. Astron., 38, 249
Rendle B. M. et al., 2019, MNRAS, 484, 771
Ricker G. R. et al., 2014, in Jr J. M. O., Clampin M., Fazio G. G., MacEwen H. A., eds, Proc. SPIE, Conf. Ser. Vol.9143, Space Telescopes and Instrumentation 2014: Optical, Infrared, and Millimeter Wave. SPIE, Bellingham, p. 556
Rogers F., Iglesias C., 1998, 135, 254
Rogers F. J., Nayfonov A., 2002, ApJ, 576, 1064
Roxburgh I. W., Vorontsov S. V., 2003, A&A, 411, 215
Salmon S. J. A. J., Van Grootel V., Buldgen G., Dupret M. A., Eggenberger P., 2021, A&A, 646, A7
Santos A. R. G. et al., 2018, ApJS, 237, 17
Santos A. R. G. et al., 2023, A&A, 672, A56
Serenelli A. et al., 2021, A&ARv, 29, 4
Silva Aguirre V., Ballot J., Serenelli A. M., Weiss A., 2011, A&A, 529, A63
Silva Aguirre V. et al., 2015, MNRAS, 452, 2127
Silva Aguirre V. et al., 2017, ApJ, 835, 173
Söderhjelm S., 1999, A&A, 341, 121
ten Brummelaar T. A. et al., 2005, ApJ, 628, 453
Thoul A. A., Bahcall J. N., Loeb A., 1994, ApJ, 421, 828

Torres G., Andersen J., Giménez A., 2010, A&ARv, 18, 67
Townsend R. H. D., Teitler S. A., 2013, MNRAS, 435, 3406
Valle G., Dell'Omodarme M., Prada Moroni P. G., Degl'Innocenti S., 2014, A&A, 561, A125
Valle G., Dell'Omodarme M., Prada Moroni P. G., Degl'Innocenti S., 2015, A&A, 575, A12
van Leeuwen F., 2007, Hipparcos, the New Reduction of the Raw Data. Vol. 350
Verma K. et al., 2014, ApJ, 790, 138
Verma K., Raodeo K., Basu S., Silva Aguirre V., Mazumdar A., Mosumgaard J. R., Lund M. N., Ranadive P., 2019, MNRAS, 483, 4678
Valle G., Dell'Omodarme M., Prada Moroni P. G., Degl'Innocenti S., 2019, Front. Astron. Space Sci., 6, 30
White T. R. et al., 2013, MNRAS, 433, 1262
White T. R. et al., 2015, in García R.A., Ballot J., eds, EPJ Web Conf. Vol. 101, The Space Photometry Revolution - CoRoT Symposium 3, Kepler KASC-7 Joint Meetin, p. 06068
Yıldız M., 2007, MNRAS, 374, 1264
Zinn J. C., Pinsonneault M. H., Huber D., Stello D., Stassun K., Serenelli A., 2019, ApJ, 885, 166

This paper has been typeset from a TEX/LATEX file prepared by the author.